

## RESEARCH ARTICLE

10.1002/2016JB013637

## Key Points:

- Lode angle affects failure stress, failure plane angle, and failure mode
- Failure-mode evolution from shear to compactive failure with mean stress in Bentheim sandstone is more prominent than in Coconino
- Predictions of failure plane angle via bifurcation theory agree qualitatively with experimental data

## Supporting Information:

- Supporting Information S1

## Correspondence to:

X. Ma,  
xma32@stanford.edu

## Citation:

Ma, X., J. W. Rudnicki, and B. C. Haimson (2017), Failure characteristics of two porous sandstones subjected to true triaxial stresses: Applied through a novel loading path, *J. Geophys. Res. Solid Earth*, 122, doi:10.1002/2016JB013637.

Received 10 OCT 2016

Accepted 15 MAR 2017

Accepted article online 20 MAR 2017

## Failure characteristics of two porous sandstones subjected to true triaxial stresses: Applied through a novel loading path

Xiaodong Ma<sup>1,2</sup> , John W. Rudnicki<sup>3</sup> , and Bezalel C. Haimson<sup>1</sup> 

<sup>1</sup>Geological Engineering Program and Department of Materials Science and Engineering, University of Wisconsin-Madison, Madison, Wisconsin, USA, <sup>2</sup>Now at Department of Geophysics, Stanford University, Stanford, California, USA, <sup>3</sup>Department of Civil and Environmental Engineering and Department of Mechanical Engineering, Northwestern University, Evanston, Illinois, USA

**Abstract** We performed an extensive suite of true triaxial experiments in two porous sandstones, Bentheim (porosity  $\approx 24\%$ ) and Coconino (17%). The experiments were conducted using a novel loading path, which maintains constant Lode angle ( $\theta$ ) throughout the test. This path enabled the examination of the effects of Lode angle and mean stress on failure ( $\sigma_{\text{oct},f}$ ). Our tests covered  $\sigma_3$  magnitudes between 0 and 150 MPa and of  $\theta$  at  $-30^\circ$  (axisymmetric extension),  $-16^\circ$ ,  $0^\circ$ ,  $+11^\circ$ ,  $+21^\circ$ , and  $+30^\circ$  (axisymmetric compression). Test results revealed the respective contribution of each of the two stress invariants to failure stress, failure plane angle, and failure mode. In both sandstones, the shear stress required for failure increases with mean stress but decreases with  $\theta$  when shear failure mode dominates. However, the dependence of failure stress on mean stress and  $\theta$  is reversed when the compactive failure mode is in control. The compactive failure mode was evident in Bentheim sandstone when compaction bands were observed under high mean stress. The Coconino sandstone did not reach the compactive failure regime within the maximum confinement applied. The failure plane angle monotonically decreases with increasing mean stress and  $\theta$ . For Coconino sandstone, failure plane angle varies between  $80^\circ$  and  $50^\circ$  for  $\sigma_{\text{oct},f}$  between 50 and 450 MPa whereas it drops to  $0^\circ$  as  $\sigma_{\text{oct},f}$  approaches 250 MPa in Bentheim sandstone. We employed the bifurcation theory to relate the stress conditions at failure to the development of failure planes. The theory is in qualitative agreement with the experimental data.

### 1. Introduction

Porous sandstones are closely related to human activities as they can host hydrocarbons, sequestered  $\text{CO}_2$ , and disposed wastewater. Failure in porous sandstones can alter the rock structure and has the potential of enhancing or slowing fluid flow in reservoirs [Holcomb and Olsson, 2003; Sternlof et al., 2004; Vajdova et al., 2004; Holcomb et al., 2007; Sun et al., 2011]. In the compressive Earth's crust, porous sandstones fail primarily due to shear or a combination of shear and compaction [Aydin et al., 2006; Eichhubl et al., 2010; Fossen et al., 2011]. Under compression, failure in porous sandstones typically takes the form of localized, tabular zones that could be generally referred to as "failure planes"; very rarely, volumetric compactive failure may occur when extremely high stresses are applied to a very weak rock [Wong and Baud, 2012].

Extensive laboratory work has been dedicated to understanding the conditions that lead to failure in porous sandstones. Practically, all these investigations were based on axisymmetric compression tests ( $\sigma_1 > \sigma_2 = \sigma_3$ ; utilizing cylindrical specimens) as reviewed by Wong and Baud [2012]. The failure characteristics were considered to depend on octahedral normal stress (or mean stress)  $\sigma_{\text{oct}}$  and octahedral shear stress  $\tau_{\text{oct}}$ . The effects of  $\sigma_{\text{oct}}$  and  $\tau_{\text{oct}}$  on failure have been thoroughly studied with respect to rock strength, deformability, and the brittle-ductile transition [Wong and Baud, 2012].

Axisymmetric extension tests ( $\sigma_1 = \sigma_2 > \sigma_3$ ), though less common, have also been used to characterize the failure of porous sandstones [Zhu et al., 1997; Bésuelle et al., 2000; Bobich, 2005]. The two types of axisymmetric tests differ in the relative values of  $\sigma_2$ , which essentially produce limiting states of deviatoric stress. The deviatoric stress state is independent of the hydrostatic stress state ( $\sigma_1 = \sigma_2 = \sigma_3$ ) and can be quantified by the Lode angle ( $\theta$ ) [Borja, 2013]. Here we use an expression of Lode angle as

$$\theta = \tan^{-1} \left\{ (\sigma_1 - 2\sigma_2 + \sigma_3) / \left[ 3^{1/2} \cdot (\sigma_1 - \sigma_3) \right] \right\} \quad (1)$$

When  $\sigma_2 = \sigma_3$ ,  $\theta = +30^\circ$ , and when  $\sigma_2 = \sigma_1$ ,  $\theta = -30^\circ$ .

A difference is generally observed in rock compressive strength between tests conducted in axisymmetric compression and those in axisymmetric extension [Haimson, 2006]. In most rocks, for the same mean stress  $\sigma_{oct}$ , the required octahedral shear stress  $\tau_{oct}$  to cause failure when  $\theta = +30^\circ$  is greater than the case when  $\theta = -30^\circ$ . This difference in  $\tau_{oct}$  can be attributed to the variation of rock failure with the deviatoric stress state or the Lode angle  $\theta$ . To fundamentally investigate the effect of Lode angle on failure, stress conditions other than  $\theta = +30^\circ$  and  $-30^\circ$  need be applied, which requires a true triaxial loading configuration ( $\sigma_1 \geq \sigma_2 \geq \sigma_3 \geq 0$ ). This configuration also simulates more realistically the stress state in the Earth's crust [Haimson, 1978; McGarr and Gay, 1978; Brace and Kohlstedt, 1980; Vernik and Zoback, 1992].

The majority of earlier true triaxial tests (also in recent modeling efforts by Duan *et al.* [2016]) were programmed so that  $\sigma_2$  and  $\sigma_3$  were maintained constant [Haimson, 2006; Mogi, 2007] (referred to here as "common" loading path). Two exceptions are the work of Ingraham *et al.* [2013] and of Makhnenko and Labuz [2014] [see also Makhnenko *et al.*, 2015; Labuz *et al.*, 2016]. The latter uses a plane-strain apparatus with passive constraint: the intermediate principal stress  $\sigma_2$  maintains the condition of minimal deformation in the out-of-plane direction and, hence, varies with increasing  $\sigma_1$ . Ingraham *et al.* [2013] control changes in all three principal stresses so that both Lode angle and mean stress are kept constant while increasing the octahedral shear stress to failure. A disadvantage of the common loading path is that all three principal stress invariants, mean stress, octahedral shear stress, and Lode angle, change throughout the test. Consequently, an alternative loading path is desired to isolate the effects of stress invariants ( $\sigma_{oct}$ ,  $\theta$ ).

In this paper, a sequel to Ma and Haimson [2016], we describe the series of true triaxial experiments in which we used a novel loading path in two porous sandstones (Coconino and Bentheim). The novel loading path enabled us to achieve a constant Lode angle (for states other than axisymmetric compression and axisymmetric extension which maintain constant Lode angle). The goal was to study the failure characteristics (in particular the stress conditions at failure and failure plane angles) as a function of Lode angle  $\theta$ , in addition to the better-known effects of  $\sigma_{oct}$  normally characterized by axisymmetric tests. We summarize failure mechanism similarities and differences between the two sandstones. We then compare our experimental data with the bifurcation theory framework by Rudnicki and Rice [1975], as extended by Rudnicki [2008, 2013] to a three-invariant model and applied by Haimson and Rudnicki [2010], which relates the stress states at failure to the failure plane angles. This comparison of theory and experiment concentrates on predicting the failure plane angle with the experimentally derived failure stress conditions and material constants.

## 2. Materials and Methods

The true triaxial tests were carried out in Coconino (17% porosity) and Bentheim (24% porosity) sandstones. These two rocks were selected because of their similar mineral content (over 95% weakly cemented quartz grains), but different porosities. Sandstones with porosities between 15 and 30% are representative of those undergoing compactive failure when subjected to high compressive stresses [Lee, 2005; Klein *et al.*, 2001]. The two selected sandstones differ in grain size, sorting, and uniaxial compressive strength. A summary of the physical properties of both sandstones can be found in Ma and Haimson [2016]. The specimens tested in this study were prepared from the same blocks as those in the series of tests reported also by Ma and Haimson [2016]. Good consistency in physical and mechanical properties was found in specimens prepared from these blocks.

The details of testing apparatus, specimen preparation, and experimental setup were reported by Ma and Haimson [2016]. In the present study, a novel loading path was adopted, with the goal of isolating the effect of stress invariants on failure. The novel loading path was designed to maintain constant the deviatoric stress state (quantified by the Lode angle  $\theta$ ). As illustrated in Figure 1, loading procedure begins with the application of all three principal stresses hydrostatically up to the desired level, and then maintaining  $\sigma_3$  constant while raising  $\sigma_1$  and  $\sigma_2$  simultaneously at a fixed stress ratio  $b (= \Delta\sigma_2/\Delta\sigma_1)$ , where  $\Delta\sigma_1 = \sigma_1 - \sigma_3$  and  $\Delta\sigma_2 = \sigma_2 - \sigma_3$  [Jimenez and Ma, 2013]. The novel loading path differs from the common loading path [Ma and Haimson, 2016] in the way  $\sigma_2$  is controlled. The novel loading path maintains a constant Lode angle  $\theta$  (equation (1)), which can be conveniently expressed in terms of the stress ratio  $b$ :

$$\theta = \tan^{-1} \left[ (1 - 2b)/3^{1/2} \right] \quad (2)$$

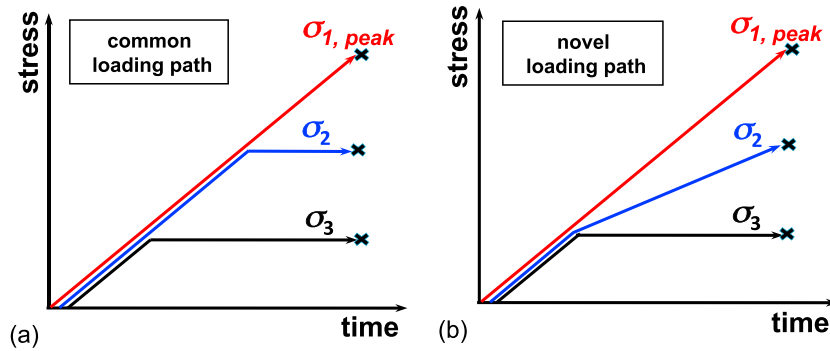


**Figure 1.** Two distinct loading paths of true triaxial testing: (a) common loading path ( $\sigma_2$  and  $\sigma_3$  constant,  $\sigma_1$  increasing monotonically) and (b) novel loading path ( $\sigma_3$  constant,  $\sigma_2$  and  $\sigma_1$  rising while maintaining constant stress ratio  $b = (\sigma_2 - \sigma_3) / (\sigma_1 - \sigma_3)$ ).

where  $b = 0$ ,  $\sigma_2 = \sigma_3$  and  $\theta = +30^\circ$ , corresponding to axisymmetric compression; where  $b = 1/2$ ,  $\sigma_2 = (\sigma_1 + \sigma_3)/2$  and  $\theta = 0^\circ$ , corresponding to deviatoric pure shear state; and where  $b = 1$ ,  $\sigma_2 = \sigma_1$ , and  $\theta = -30^\circ$ , corresponding to axisymmetric extension (Table 1).

The mean stress and octahedral shear stresses can also be expressed in terms of  $\sigma_3$ ,  $\Delta\sigma_1$ , and  $b$ :

$$\sigma_{oct} = (\sigma_1 + \sigma_2 + \sigma_3)/3 = \sigma_3 + (1 + b) \cdot \Delta\sigma_1/3 \tag{3a}$$

$$\tau_{oct} = [(\sigma_1 - \sigma_2)^2 + (\sigma_2 - \sigma_3)^2 + (\sigma_3 - \sigma_1)^2]^{1/2}/3 = [2(b^2 - b + 1)]^{1/2} \cdot \Delta\sigma_1/3 \tag{3b}$$

Ma and Haimson [2016] identified the effect of the stress ratio  $b$  on failure using the common loading path. Experiments using the novel loading path (constant  $b$ ) enabled the study of the octahedral shear stress at failure ( $\tau_{oct,f}$ ) as a function of the mean stress at failure ( $\sigma_{oct,f}$ ) for different constant Lode angles ( $\theta$ ).

In Coconino sandstone the applied constant Lode angle  $\theta$  values were  $+30^\circ$ ,  $+21^\circ$ ,  $+11^\circ$ ,  $0^\circ$ , and  $-30^\circ$ . For each constant Lode angle, the applied constant  $\sigma_3$  magnitudes were 0, 10, 20, 50, 80, 100, 120, and 150 MPa, same as those used in the common loading path tests reported by Ma and Haimson [2016]. For Bentheim sandstone, the applied constant Lode angle  $\theta$  values were  $+30^\circ$ ,  $+21^\circ$ ,  $+11^\circ$ ,  $0^\circ$ ,  $-16^\circ$ , and  $-30^\circ$ , and the applied constant  $\sigma_3$  were 0, 8, 15, 30, 60, 80, 120, and 150 MPa. A complete list of test data is given in Table 2.

### 3. Experimental Results

#### 3.1. True Triaxial Failure Stress

Figure 2 shows the variation of  $\tau_{oct,f}$  with  $\sigma_{oct,f}$  in the two sandstones for each tested Lode angle ( $\theta$ ). The relationship  $\tau_{oct,f}$  versus  $\sigma_{oct,f}$  for each constant  $\theta$  is well fitted by a second-order polynomial equation (detailed in equations (A1) and (A3), Text S1 in the supporting information). Common to both sandstones,  $\tau_{oct,f}$  first rose with  $\sigma_{oct,f}$ , though at a ever decreasing rate. The  $\theta = +30^\circ$  curve ( $\sigma_2 = \sigma_3$ , or axisymmetric compression) rose with  $\sigma_{oct,f}$  at the steepest slope ( $d\tau_{oct,f}/d\sigma_{oct,f}$ ) at low  $\sigma_{oct,f}$ , but its slope dropped considerably as  $\sigma_{oct,f}$  was increased (Figure 2). As  $\theta$  varied from  $+30^\circ$  (axisymmetric compression) to  $0^\circ$  (deviatoric pure shear) and then to  $-30^\circ$  ( $\sigma_2 = \sigma_1$  or axisymmetric extension), the  $\sigma_{oct,f}$  magnitude required for failure typically increased for a constant  $\tau_{oct,f}$ . Unlike Coconino sandstone,  $\tau_{oct,f}$  in Bentheim eventually reached a peak and started declining when  $\sigma_{oct,f}$  approached 200 MPa, forming a "cap" [Olsson, 1999]. The  $\sigma_{oct,f}$  magnitude when the peak of each constant  $\theta$  trend was reached gradually increased as Lode angle  $\theta$  varied from  $+30^\circ$  to  $-30^\circ$ . These differences showed that Bentheim sandstone's  $\sigma_{oct,f}$  magnitude required for failure at the same  $\tau_{oct,f}$  typically decreased as  $\theta$  varied from  $+30^\circ$  to  $-30^\circ$ , reversing the trend before the peak was reached.

**Table 1.** Correspondence of the Applied Stress Ratio to the Lode Angle

Stress Ratio, $b$	Lode Angle, $\theta$	Deviatoric Stress State
1:1	$-30^\circ$	Axisymmetric extension
3:4	$-16^\circ$	-
1:2	0	Deviatoric pure shear
1:3	$+11^\circ$	-
1:6	$+21^\circ$	-
0	$+30^\circ$	Axisymmetric compression

**Table 2.** The State of Stress at Failure and the Failure Plane Angle Obtained From True Triaxial Tests in Coconino and Bentheim Sandstone Under Stress Control Mode

$\sigma_3$ (MPa)	$\sigma_2$ (MPa)	$\sigma_{1,peak}$ (MPa)	$\theta^a$ (deg)	$\theta^{Tb}$ (deg)
<i>Coconino Sandstone</i>				
<i><math>\theta = +30^\circ</math>, Axisymmetric Compression</i>				
0.0	0.0	56.1	75.0	74.3
10.0	10.0	161.8	68.3	70.4
20.0	20.0	235.2	68.7	67.5
50.0	50.0	347.2	61.7	62.2
80.0	80.0	427.7	60.1	57.8
100.0	100.0	465.2	55.5	55.4
120.0	120.0	506.4	50.2	52.9
150.0	150.0	565.2	50.0	49.2
<i><math>\theta = +21^\circ</math></i>				
0.0	14.5	87.2	80.0	72.1
10.0	41.0	194.3	75.5	68.8
20.0	61.9	269.2	72.0	66.1
50.0	103.1	363.6	65.5	61.9
80.0	145.1	463.7	61.1	57.4
100.0	169.3	507.6	54.5	55.1
120.0	192.0	539.8	53.6	53.1
150.0	230.2	619.9	53.2	49.2
<i><math>\Delta\sigma_2/\Delta\sigma_1 = 1/3</math> (<math>\theta = +11^\circ</math>)</i>				
0.0	26.9	80.4	80.0	75.6
10.0	72.0	194.4	76.0	71.8
20.0	97.6	249.4	70.5	69.6
50.0	160.1	375.3	65.4	64.0
80.0	207.4	456.0	59.0	59.9
100.0	236.7	503.7	56.5	57.3
120.0	262.8	541.2	55.6	55.1
150.0	303.0	601.2	52.8	51.7
<i><math>\theta = 0^\circ</math>, Deviatoric Pure Shear</i>				
0.0	46.8	94.1	79.9	80.1
10.0	101.3	190.5	76.0	75.8
20.0	132.7	243.1	73.8	73.1
30.0	174.8	315.5	68.5	69.7
40.0	196.3	348.0	69.0	67.8
45.0	199.4	348.4	69.1	67.6
50.0	212.0	368.4	67.1	66.6
60.0	241.1	416.0	65.0	64.1
70.0	249.4	422.9	61.7	63.4
80.0	279.5	472.4	57.7	60.8
100.0	324.4	540.8	54.3	57.1
120.0	341.1	556.5	54.2	55.5
150.0	403.2	648.0	54.1	50.4
<i><math>\theta = -30^\circ</math>, Axisymmetric Extension</i>				
0.0	76.8	76.8	80.3	90.0
10.0	170.9	170.9	76.9	90.0
20.0	225.9	225.9	71.0	80.5
50.0	341.3	341.3	66.8	69.5
80.0	429.9	429.9	62.0	62.3
100.0	493.6	493.6	59.5	57.4
120.0	527.8	527.8	57.0	54.5
150.0	620.7	620.7	56.0	47.5

**Table 2.** (continued)

$\sigma_3$ (MPa)	$\sigma_2$ (MPa)	$\sigma_{1,peak}$ (MPa)	$\theta^a$ (deg)	$\theta^{Tb}$ (deg)
<i>Bentheim Sandstone</i>				
$\theta = +30^\circ$ , Axisymmetric Compression				
0.0	0.0	30.0	86.0	77.4
8.0	8.0	85.1	71.0	75.8
15.0	15.0	122.4	69.0	73.3
30.0	30.0	187.6	63.0	66.2
50.0	50.0	238.1	57.0	55.8
60.0	60.0	251.6	51.0	51.4
80.0	80.0	273.0	42.0	41.8
100.0	100.0	285.2	40.0	32.2
120.0	120.0	315.0	13.0	18.1
150.0	150.0	329.1	0.0	2.3
$\theta = +21^\circ$				
15.0	36.7	135.7	62.0	69.6
30.0	57.1	190.6	66.0	63.4
60.0	93.3	255.5	53.0	49.1
80.0	112.6	271.0	49.0	41.5
120.0	156.6	331.8	20.0	21.8
150.0	182.8	342.4	0.0	21.3
$\theta = +11^\circ$				
15.0	57.1	141.0	69.0	70.1
30.0	87.2	199.3	67.0	63.9
60.0	130.9	269.0	51.0	50.4
80.0	160.0	315.8	45.0	39.2
120.0	191.7	330.7	29.0	30.3
150.0	217.5	349.0	5.0	27.0
$\theta = 0^\circ$ , Deviatoric Pure Shear				
0.0	16.5	32.7	84.0	76.9
8.0	53.7	99.0	72.0	75.5
15.0	71.8	128.3	69.0	74.1
30.0	117.5	202.0	66.0	68.2
50.0	140.3	228.2	63.0	63.3
60.0	176.0	289.2	58.0	53.1
80.0	193.3	305.3	48.0	46.6
100.0	207.1	310.5	37.0	41.6
120.0	226.0	328.9	34.0	32.9
150.0	258.5	363.5	15.0	14.9
$\theta = -16^\circ$				
15.0	103.3	132.5	70.0	83.4
30.0	162.2	204.9	67.0	77.7
60.0	223.2	274.1	58.0	61.0
80.0	223.3	268.5	48.0	58.6
120.0	275.5	323.7	38.0	22.3
150.0	290.8	334.2	10.0	0.0
$\theta = -30^\circ$ , Axisymmetric Extension				
0.0	39.3	39.3	80.0	90.0
8.0	84.5	84.5	72.0	90.0
15.0	119.5	119.5	70.0	90.0
30.0	181.6	181.6	66.0	90.0
50.0	237.9	237.9	59.0	71.9
60.0	274.8	274.8	55.0	55.2
80.0	285.4	285.4	53.0	44.9
100.0	320.1	320.1	52.0	0.0
120.0	306.2	306.2	25.0	11.7
150.0	346.3	346.3	2.0	0.0

<sup>a</sup> $\theta$  is the failure plane angle, defined as the angle between the  $\sigma_1$  direction and the normal to the average failure plane.  
<sup>b</sup> $\theta^T$  is the theoretically predicted failure plane angle based on the known stress condition at failure.

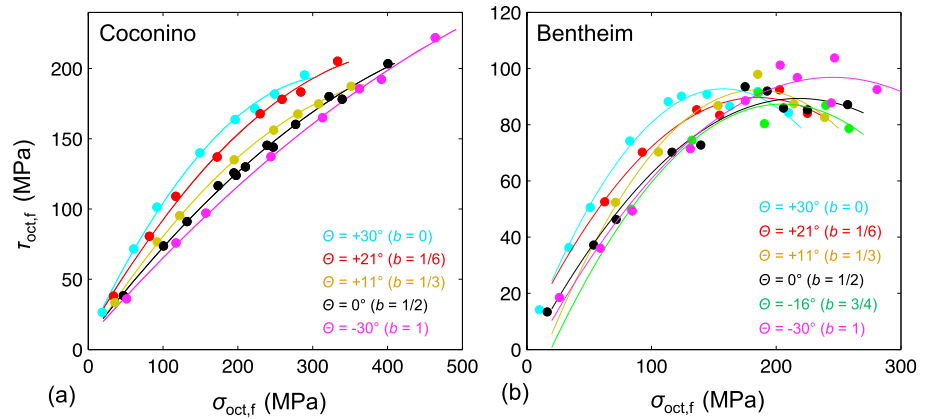


**Figure 2.** Variation of the octahedral shear stress at failure ( $\tau_{oct,f}$ ) with the mean stress at failure ( $\sigma_{oct,f}$ ) for all constant Lode angles in Coconino and Bentheim sandstones.

The results in Figure 2 are consistent with previous results for axisymmetric extension and axisymmetric compression showing that  $\tau_{oct,f}$  is greater for the latter than the former at the same value of  $\sigma_{oct,f}$  in the brittle regime. (This trend reverses for the ductile regime,  $\tau_{oct,f}$  decreasing with  $\sigma_{oct,f}$  but previous results are generally limited to the brittle regime). These include tests on Vosges sandstone by *Bésuelle et al.* [2000], Berea sandstone by *Bobich* [2005] and *Makhnenko et al.* [2015], Indiana limestone by *Labuz et al.* [2016], and on a handful of crystalline rocks (e.g., Westerly granite by *Mogi* [2007]). Nonetheless, the appreciable effect of  $\theta$  reveals that the  $\tau_{oct,f}$ - $\sigma_{oct,f}$  relationship obtained from axisymmetric tests are limiting cases only. The inclusion of test conditions at Lode angles other than  $\pm 30^\circ$  is necessary to formulate an adequate three-dimensional failure description [e.g., *Makhnenko et al.*, 2015; *Labuz et al.*, 2016]. Furthermore, our novel true triaxial tests confirmed that the dispersion of  $\tau_{oct,f}$ - $\sigma_{oct,f}$  trend based on the common true triaxial tests [*Ma and Haimson*, 2016] is largely due to the dependence on the Lode angle  $\theta$  (or the stress ratio  $b$ ) [*Haimson et al.*, 2016].

The strong dependence on Lode angle is also consistent with the true triaxial results of *Ingraham et al.* [2013] on Castlegate sandstone in which they keep both Lode angle and  $\sigma_{oct,f}$  constant. As in the results here they find that  $\tau_{oct,f}$  increases with Lode angle  $\theta$  for fixed  $\sigma_{oct,f}$  in the brittle regime with the trend reversing in the ductile regime. Even though the Castlegate sandstone is slightly more porous than the Bentheim sandstone (26% versus 24%), it undergoes that brittle-ductile transition at a much lower mean stress. In particular the transition for the Castlegate occurs at about 120 MPa versus about 180 MPa for the Bentheim. It is likely that the presence of clay minerals in the Castlegate further weakens its quartz-supported framework.

*Makhnenko et al.* [2015] and *Labuz et al.* [2016] augment their axisymmetric compression and extension tests with true triaxial tests in a plane strain apparatus [*Makhnenko and Labuz*, 2014]. These tests give results for Lode angles intermediate to axisymmetric compression ( $30^\circ$ ) and axisymmetric extension ( $-30^\circ$ ). As noted earlier, these tests do not generally maintain constant Lode angle and values of the Lode angle are not reported. Figure 4b of *Makhnenko et al.* [2015] and Figure 7 of *Labuz et al.* [2016] indicate that the Lode angles at failure are different for different mean stresses. They model these results by using a pyramidal *Paul-Mohr-Coulomb* failure surface with planar facets [*Meyer and Labuz*, 2013].

### 3.2. Failure Planes

Failure in both sandstones generally occurred along localized planes of concentrated deformation striking in the  $\sigma_2$  direction. Depending on the magnitude of the applied confinement, the failure plane could be a fault (or shear band) or even a compaction band (in Bentheim sandstone subjected to high  $\sigma_3$ ). Although the failure planes are locally irregular, their overall orientation can be characterized by a failure plane angle,  $\theta$ , measured between the normal to the plane and the  $\sigma_1$  direction. Failure plane angles  $\theta$  in both sandstones are plotted in Figure 3 as a function of  $\sigma_{oct,f}$  for each constant Lode angle  $\theta$ . The rise in either  $\sigma_{oct,f}$  or  $\theta$  led to the decrease in  $\theta$ . In Coconino sandstone, the failure plane angle  $\theta$  decreased from approximately  $80^\circ$  at the lowest  $\sigma_{oct,f}$  ( $\approx 50$  MPa) to about  $50^\circ$  as  $\sigma_{oct,f}$  approached 350 MPa. This variation of  $\theta$  with  $\sigma_{oct,f}$  for each constant Lode angle series was fitted by a linear relationship (detailed in equation (A2), Text S1). In Bentheim sandstone, the failure plane angle  $\theta$  dropped monotonically from approximately  $85^\circ$  at the

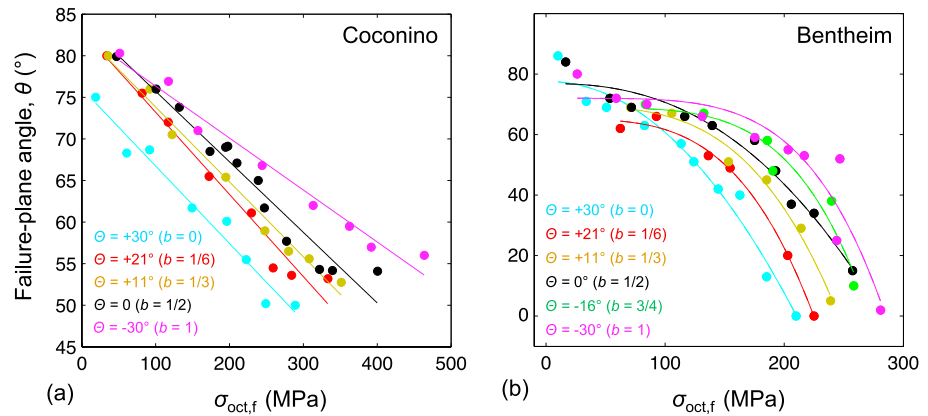


**Figure 3.** Variation of the failure plane angle ( $\theta$ ) with the mean stress at failure ( $\sigma_{oct,f}$ ) for all constant Lode angles in Coconino and Bentheim sandstones.

lowest  $\sigma_{oct,f}$  ( $\approx 15$  MPa) to about  $0^\circ$  as  $\sigma_{oct,f}$  approached 200 MPa. The trend could be well fitted by a power law equation (detailed in equation (A4), Text S1). For the same  $\sigma_{oct,f}$ , failure plane angle increased by up to  $16^\circ$  in Coconino sandstone and by nearly  $60^\circ$  in Bentheim sandstone as the Lode angle  $\theta$  varied from  $+30^\circ$  to  $-30^\circ$  (corresponding to the stress ratio  $b$  rising from 0 to 1).

The evolution of failure plane angle  $\theta$  and failure mode with  $\sigma_{oct,f}$  for a constant  $\theta$  ( $=0^\circ$ ) is clearly shown in photographs of  $\sigma_1$ - $\sigma_3$  sections of tested specimens (Figure 4). The development of multiple parallel and conjugate shear bands in both sandstones and the emergence of compaction bands in Bentheim sandstone demonstrate the brittle-ductile transition [Paterson and Wong, 2005, pp. 213–217]. (Additional tests characterizing the rocks’ deformability and the brittle-ductile transition can be found in Text S3). These observations offer insights to the test results via the common loading path by Ma and Haimson [2016] in that the apparent variations of angle  $\theta$  with principal stresses can be plausibly attributed to the variations with  $\sigma_{oct,f}$  and  $\theta$ . Our

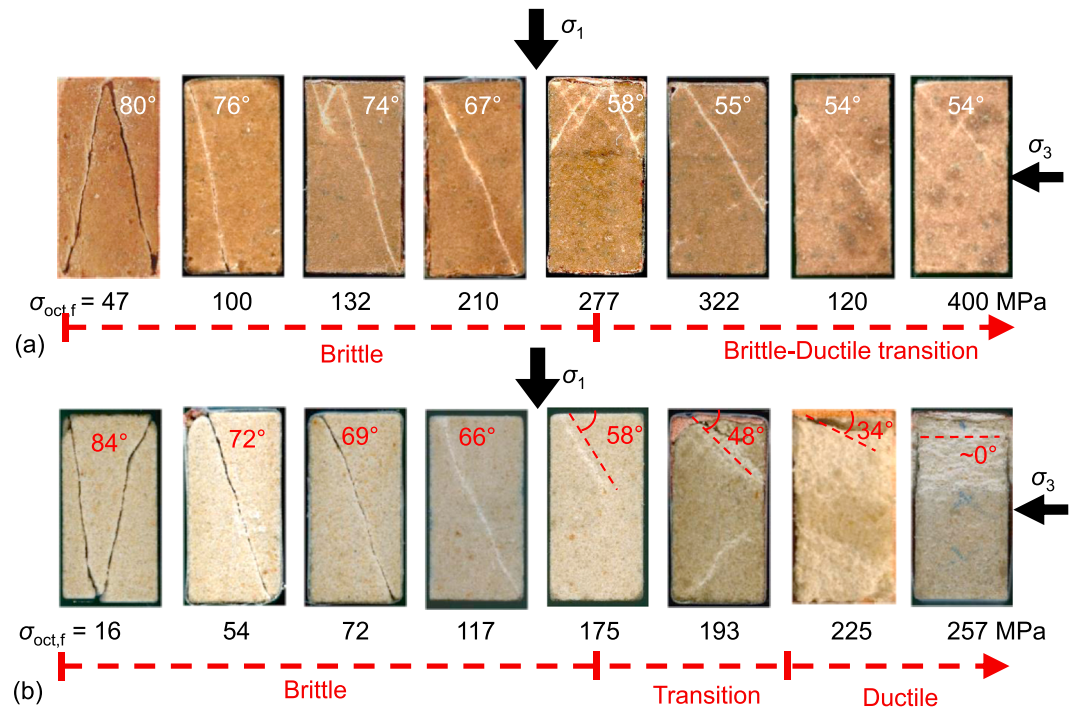


**Figure 4.** Photographs of (a) Coconino and (b) Bentheim sandstone specimens tested under the novel loading path (at deviatoric pure shear stress state,  $b = 1/2$  or  $\theta = 0^\circ$ ): the failure planes shown on the samples’  $\sigma_1$ - $\sigma_3$  surfaces demonstrate that the failure plane angle decreases and the failure mode evolves with  $\sigma_{oct,f}$ .

test results are also consistent with the observations by *Ingraham et al.* [2013], although as mentioned earlier they use loading paths that maintain both a constant octahedral normal stress and Lode angle.

#### 4. The Application of Bifurcation Theory to True Triaxial Failure Data

Different theories have been advanced to describe failures like those observed in the two tested sandstones. *Rudnicki and Rice* [1975] proposed that failure, in which strain localization develops, can be described as a bifurcation from homogeneous deformation. Specifically, failure is predicted to occur as a result of strain localization with concentrated deformation along a plane as opposed to uniform deformation of the intact rock. As an immediate precursor to failure or as a final form of failure, the predicted localized planar structure resembles the resulting failure plane observed in the laboratory and in the field. In addition, the predicted failure planes strike in the  $\sigma_2$  direction and dip toward  $\sigma_3$ , as verified by experiments. The stress conditions upon failure and rock constitutive parameters affect the appearance and inclination of the predicted failure plane (i.e., failure plane angle  $\theta$ ), as observed in experiments [*Wong and Baud*, 2012]. In principle, the bifurcation theory could be used to predict the onset of failure and the accompanying failure plane angle although the required input constitutive parameters are difficult to measure. The failure description by *Rudnicki and Rice* [1975] was originally developed for dilatant materials, but it was further extended to be suitable for the full spectrum of failure planes varying between end members of  $0^\circ$  and  $90^\circ$  [*Ottosen and Runesson*, 1991; *Bésuelle and Rudnicki*, 1997; *Rudnicki and Olsson*, 1998; *Bésuelle*, 2001; *Issen and Rudnicki*, 2000; *Wong and Baud*, 2012].

The bifurcation theory was previously employed to compare results with experimental observations of failure plane angle in Westerly granite [*Rudnicki*, 2008, 2013] and TCDP siltstone [*Haimson and Rudnicki*, 2010]. Although the bifurcation theory can describe the stress state at the onset of failure and the failure plane angle, comparison with the experimental data has concentrated on the failure plane angle, where the required constitutive parameters are fewer. These comparisons have, however, been largely confined to the limited existing experimental data of the Lode angle equal to either  $+30^\circ$  (axisymmetric compression) or  $-30^\circ$  (axisymmetric extension). This is particularly unfortunate because the theory is known to have deficiencies in these two limiting states [*Bésuelle and Rudnicki*, 1997; *Rudnicki and Olsson*, 1998; *Haimson and Rudnicki*, 2010]. To that end, true triaxial tests conducted at fixed Lode angles between the two axisymmetric states, as reported in this study, should provide a more convincing comparison between experimental data and theory.

##### 4.1. Relating Failure Stress Conditions to Failure Plane Angle Via Bifurcation Theory

According to the *Coulomb* theory, the failure plane angle ( $\theta$ ) is related to a material parameter called coefficient of internal friction ( $\mu_i$ ), as follows:

$$\theta = \pi/4 + \tan^{-1}(\mu_i)/2 \quad (4)$$

In the *Coulomb* theory the internal friction coefficient  $\mu_i$  is considered a constant of the material. Thus, the failure plane angle is also assumed to be constant. However, the novel loading path tests in Coconino and Bentheim sandstones have clearly demonstrated that the failure plane angle ( $\theta$ ) is variable and is a function of the stress conditions. The variation of  $\theta$  with the stress conditions requires a generalized expression to describe this relationship. *Rudnicki and Rice* [1975] gave an expression for the angle  $\theta$ , but it was then rewritten by *Rudnicki and Olsson* [1998] into the form that is comparable to that of the *Coulomb* theory:

$$\theta = \pi/4 + \arcsin(\alpha)/2 \quad (5)$$

where  $\alpha$  is a function of multiple material parameters (see equation (6)) and the Lode angle. The two end-members of failure planes occur when  $\alpha$  is either  $-1$  or  $+1$ . When  $\alpha \geq 1$ ,  $\theta = 90^\circ$ , corresponding to the failure mode of axial splitting or the opening of dilation bands [*Du Bernard et al.*, 2002]; when  $\alpha \leq -1$ ,  $\theta = 0^\circ$ , corresponding to the failure mode of pure compaction bands [*Mollema and Antonellini*, 1996; *Sternlof et al.*, 2005; *Eichhubl et al.*, 2010; *Fossen et al.*, 2011].

Given the knowledge of failure plane angle variation with stress conditions, equation (5) could be employed for some stress states to infer the unknown material parameters that control the value of  $\alpha$ . Subsequently, the constrained equation (5) could be utilized to predict the failure plane angle for any other stress conditions.

The prediction of failure plane angle using the bifurcation theory is strongly dependent on the type of constitutive relation used. *Rudnicki and Rice* [1975] and *Rudnicki and Olsson* [1998] employed a

two-invariant yield description, i.e., one that depends on the Mises equivalent stress,  $\tau_{\text{Mises}} = (3/2)^{1/2} \tau_{\text{oct}}$  and the mean stress,  $\sigma_{\text{oct}}$ , but not on the Lode angle ( $\theta$ ). An expression for the parameter  $\alpha$  in equation (5), equivalent to that used by *Rudnicki and Olsson* [1998], is

$$\alpha = \frac{2\sqrt{3/2}(1+\nu)(\beta+\mu)/3 - N(1-2\nu)}{\sqrt{4-3N^2}} \quad (6)$$

where  $N = 2\sin\theta/3^{1/2}$ ,  $\mu$  is a friction coefficient, and  $\beta$  is a dilatancy factor. The additional factor of  $(3/2)^{1/2}$  in the first term of equation (6), by comparison with the expression of *Rudnicki and Olsson* [1998], arises because of the use of  $\tau_{\text{oct}}$  rather than the Mises equivalent stress, consistent with what is used elsewhere in the paper; more specifically,  $\mu = d\tau_{\text{oct}}/d\sigma_{\text{oct}}$ . This requires that the corresponding definition of  $\beta$  be modified. The dilatancy factor  $\beta$  is the ratio of the plastic volume strain increment to plastic shear strain increment,  $-d\varepsilon^p/d\gamma^p$ , where  $d\varepsilon^p [= d\varepsilon_{11}^p + d\varepsilon_{22}^p + d\varepsilon_{33}^p]$  and  $d\gamma^p [= \sqrt{3de_{ij}^p \cdot de_{ij}^p}]$  ( $de_{ij}^p = d\varepsilon_{ij}^p - \delta_{ij}d\varepsilon^p/3$ ). The minus sign in the definition of  $\beta$  arises because strains are taken as positive in compression here. Consequently,  $\beta$  is positive for dilation and negative for compaction. The factor of 3 in the expression for  $de_{ij}^p$  differs from the factor of 2 in the corresponding expression of *Rudnicki and Rice* [1975] in order to make the definition of  $\beta$  consistent with the definition of  $\mu$  in terms of  $\tau_{\text{oct}}$ . The frictional coefficient  $\mu$  is the slope of the yield surface and when  $\mu = \beta$ , the plastic potential is the same as the yield function. In compactive, porous rocks, for low-to-moderate confinement,  $\mu > 0$ ; for higher confinement,  $\mu < 0$ .

The two-invariant model and equation (6), or its equivalent, were used to model the failure plane angle variations by *Rudnicki and Olsson* [1998] for Castlegate sandstone, by *Rudnicki* [2008] for Westerly granite, and by *Ma* [2014] for Coconino and Bentheim sandstones. However, in no case was the agreement between the theoretical predictions and experimental results satisfactory. Consequently, an analysis incorporating a three-invariant model, introduced by *Rudnicki* [2008] and detailed by *Rudnicki* [2013], is used here. In particular, the yield function is given by  $F(\tau_{\text{oct},f}, \sigma_{\text{oct},f}, \theta) = 0$  and plastic potential by  $G(\tau_{\text{oct},f}, \sigma_{\text{oct},f}, \theta) = 0$ , where the subscript “ $f$ ” denotes the value at failure. (*Rudnicki* [2008, 2013] used  $\tau_{\text{Mises}} = (3/2)^{1/2} \tau_{\text{oct}}$  and  $\sigma_{kk} = -3\sigma_{\text{oct}}$ ). As a consequence yield and material parameters such as the frictional coefficient  $\mu$  and the dilatancy factor  $\beta$  are dependent on  $\theta$ .

*Rudnicki* [2008] gave an expression for the failure plane angle for yield and plastic potential functions depending on all three invariants and noted that *Ottosen and Runesson* [1991] had previously given an equivalent expression. *Rudnicki* [2013] gave some details of the derivation of this result and noted that it could be obtained by substitution for parameters in the two invariant result of *Rudnicki and Olsson* [1998] (equation (6) here). The result (modified from equation (28) of *Rudnicki* [2013]) is

$$\alpha = \frac{(-1/\sqrt{6})(1+\nu) \cdot \cos\phi \cdot (F_\sigma + G_\sigma)/F_\tau - (1-2\nu) \cdot \sin(\phi + \theta)/\sqrt{3}}{\cos(\phi + \theta)} \quad (7)$$

where

$$\tan\phi = F_\theta/(\tau \cdot F_\tau) \quad (8)$$

Here and in what follows, for simplicity of notations, the subscripts  $\sigma$  and  $\tau$  denote partial derivatives with respect to  $\sigma_{\text{oct},f}$  and  $\tau_{\text{oct},f}$ . Differences from *Rudnicki* [2008, 2013] in the numerical factor and sign of the first term of equation (7) again result from taking stresses and strains as positive in compression and from using  $\tau_{\text{oct}} = (2/3)^{1/2} \tau_{\text{Mises}}$  and  $\sigma_{kk} = -3\sigma_{\text{oct}}$ . As explained by *Rudnicki* [2008, 2013] and *Haimson and Rudnicki* [2010], the expression assumes that normals to the yield surface and plastic potential coincide (flow is associated) in the deviatoric planes (perpendicular to the hydrostatic axis) requiring that  $F_\sigma = G_\sigma$  and that  $F_\tau = G_\tau$ . There is ample observational evidence and theoretical basis for nonassociated flow in meridian planes (planes containing the hydrostatic axis). Because there is neither observational evidence nor theoretical basis for nonassociated flow in deviatoric planes, this assumption is reasonable. A consequence of this assumption is that  $G$  can differ from  $F$  only by a function of mean stress  $H(\sigma)$ . Therefore  $G_\sigma$  must have the following form:

$$G_\sigma = F_\sigma + H'(\sigma) \quad (9)$$

$\phi$  is the angle between the normal to the failure surface on the deviatoric plane (i.e., the  $\tau_{\text{oct}}-\theta$  section) and a radial vector. A nonzero  $\phi$  implies the shape of the failure surface in the deviatoric plane is not

circular as in a *Drucker-Prager* model and the radius depends on the Lode angle. If  $\phi=0$ , equation (7) reduces to

$$\alpha = \frac{(-1/\sqrt{6})(1+\nu) \cdot (F_\sigma + G_\sigma)/F_\tau - (1-2\nu) \cdot \sin\theta/\sqrt{3}}{\cos\theta} \quad (10)$$

which is equivalent to the two-invariant version (equation (6)). For the three invariant model the friction coefficient  $\mu$  and the dilatancy factor  $\beta$  can be related to  $F$ ,  $G$ , and  $\phi$ :

$$\beta = -G_\sigma \cdot \cos\phi / F_\tau \quad (11a)$$

$$\mu = -F_\sigma \cdot \cos\phi / F_\tau \quad (11b)$$

(These results follow from *Rudnicki* [2013] by using equations (25)–(27) in the substitutions for  $\mu$  and  $\beta$  preceding equation (28) with, again, taking account of the difference in sign and definitions used here.)

For  $F(\tau_{\text{oct},f}, \sigma_{\text{oct},f}, \theta) = 0$ , we adopted the yield description proposed by *Rudnicki* [2013]:

$$F(\tau_{\text{oct},f}, \sigma_{\text{oct},f}, \theta) = -\sqrt{\frac{4}{27}} A \cdot \sin(3\theta) \cdot \left(\frac{\tau_{\text{oct},f}}{\tau_{\text{oct},0}}\right) + \left(\frac{\tau_{\text{oct},f}}{\tau_{\text{oct},0}}\right)^2 - 1 = 0 \quad (12)$$

Equation (12) is modified and generalized from failure criteria proposed by *Matsuoka and Nakai* [1974] and *Lade and Duncan* [1975]. It was introduced by *Rudnicki* [2013] and used by *Haimson and Rudnicki* [2010] as a yield description. We use it here as such, but it has been used as a failure condition by *Ma* [2014], *Ma et al.* [2014], *Rudnicki* [2016], and *Ma et al.* [2017]. As remarked by *Rudnicki* [2013], yield data at failure are generally not available for rocks. In the absence of such data, we follow *Rudnicki* [2013] and *Haimson and Rudnicki* [2010] and use the failure data to infer the form of equation (12). Then the failure plane angle is predicted using equation (7).

When  $\theta=0$ , the first term of equation (12) vanishes and the equation reduces to  $\tau_{\text{oct},\theta=0} = \tau_{\text{oct},0}(\sigma_{\text{oct},f})$ , so that  $\tau_{\text{oct},0}$  represents the dependence of  $\tau_{\text{oct},f}$  on  $\sigma_{\text{oct},f}$  under the deviatoric pure shear stress state ( $\theta=0^\circ$ ) (the subscript “0” denotes  $\theta=0^\circ$ ). The values of  $A$  are limited to between  $-1$  and  $+1$  so that equation (12) has real roots.  $A$  characterizes the discrepancy of failure (in the form of  $\tau_{\text{oct},f}$ ) between axisymmetric compression and axisymmetric extension states ( $\sigma_2=\sigma_3$  and  $\sigma_2=\sigma_1$ ) for a constant  $\sigma_{\text{oct},f}$ . The discrepancy, if any, reveals the dependence of  $\tau_{\text{oct},f}$  on Lode angle  $\theta$ . When  $A=0$ , the first term in equation (12) vanishes, and the equation is reduced to  $\tau_{\text{oct},f} = \tau_{\text{oct},0}(\sigma_{\text{oct},f})$ , implying no failure ( $\tau_{\text{oct},f}$ ) variation with  $\theta$ . Specifically, the novel test data series of  $\theta=0^\circ$  was used to determine the expressions of  $\tau_{\text{oct},0}$  as a function of  $\sigma_{\text{oct},f}$ . Then  $A$  corresponding to each data point ( $\tau_{\text{oct},f}, \sigma_{\text{oct},f}$ ) can be calculated by inserting  $\tau_{\text{oct},0}$  into equation (12) (for details, see *Ma* [2014], *Ma et al.* [2014], and *Ma et al.* [2017]).

The three-invariant model incorporates the dependence of  $F=0$  and  $G=0$  on the Lode angle  $\theta$ . It suggests the necessity of using the data of two constant Lode angle test series to constrain the  $\theta$  dependence. Here we follow the prediction process by *Haimson and Rudnicki* [2010]: the novel test series for axisymmetric compression ( $\theta=+30^\circ$ ) and deviatoric pure shear ( $\theta=0^\circ$ ) were used to constrain the dependence of  $\theta$  on failure plane angle. Based on the experimentally obtained angle variation with  $\sigma_{\text{oct},f}$  under these two constant Lode angles, the parameters in  $F=0$  and  $G=0$  could be determined and the exact form of  $F$  and  $G$  used in equation (5) for the angle prediction under any other Lode angles. Detailed derivations regarding forms of  $F$  and  $G$  are shown in Text S2.

First, the experimentally obtained variations of failure plane angle  $\theta$  with  $\sigma_{\text{oct},f}$  at axisymmetric compression ( $\theta=+30^\circ$ ) (equation (A2a)) and deviatoric pure shear ( $\theta=0^\circ$ ) (equation (A2d)) were substituted into equation (5) to generate the variation with  $\sigma_{\text{oct},f}$  of two unknown functions:  $H'(\sigma) \cdot \tau_0$  (equation (B24)) and  $d\tau_0/d\sigma$  (equation (B25)). They led to the determination of frictional coefficient ( $\mu$ ) and dilatancy factor ( $\beta$ ) as described by equation (11). For Coconino sandstone, *Poisson's* ratio  $\nu=0.25$  [*Ma and Haimson*, 2016] and parameter  $A=0.6$  [*Ma*, 2014] for failure description  $F=0$  (equation (7)) were used. For Bentheim sandstone, *Poisson's* ratio  $\nu=0.36$  [*Ma and Haimson*, 2016] and  $A=0.33$  [*Ma*, 2014]. The observations in *Ma et al.* [2014, 2017] indicated that  $A$  depends on  $\sigma_{\text{oct},f}$ . The data were described roughly by a linear variation. Here for simplicity,  $A$  in the yield description  $F=0$  was taken to be a constant equal to the average values of the linear variation.

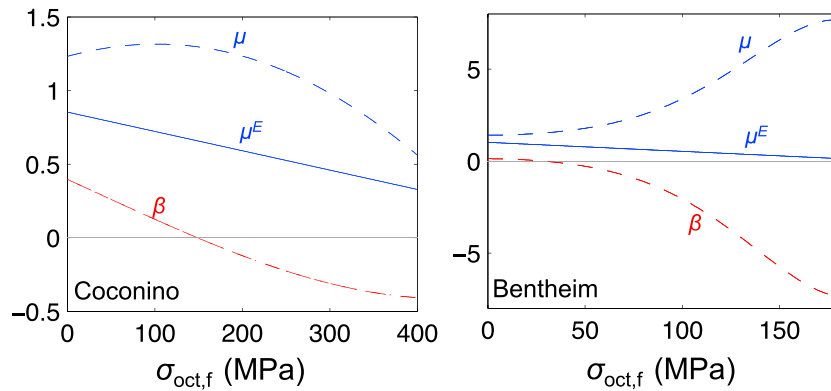


**Figure 5.** Variation with  $\sigma_{\text{oct},f}$  in Coconino and Bentheim sandstones of the inferred dilatancy factor  $\beta$  and frictional coefficient  $\mu$  based on the three-invariant model, and the empirically fitted  $\mu^E$  based on the experimental data under deviatoric pure shear ( $\theta = 0^\circ$ ).

At deviatoric pure shear ( $\theta = 0^\circ$ ),  $\mu$  and  $\beta$  corresponding to equation (11) are given by

$$\mu_{\theta=0} = \frac{1}{\sqrt{1 + A^2/3}} \frac{d\tau_0}{d\sigma} \quad (13a)$$

$$\beta_{\theta=0} = \frac{1}{\sqrt{1 + A^2/3}} \left\{ \frac{d\tau_0}{d\sigma} - H'(\sigma) \cdot \tau_0 / 2 \right\} \quad (13b)$$

(The expression for  $\beta$ , equation (13b) corrects the misprint of a factor of 3 and the sign of equation (17) of Haimson and Rudnicki [2010]) as derived from equation (11a) and more in Text S2). The derived variations of  $d\tau_0/d\sigma$ , which is a frictional coefficient at pure shear ( $\theta = 0^\circ$ ), are shown in Figure 5. (Note that only when  $A = 0$ , for a Drucker-Prager material, does  $d\tau_0/d\sigma$  correspond to the actual friction coefficient for the three-invariant model at pure shear although for  $A = 0.6$  or  $0.33$  the numerical difference is small.) We also included the experimentally obtained frictional coefficient  $\mu^E [=d\tau_{\text{oct},f}/d\sigma_{\text{oct},f}]$  (based on failure stress data from equation (A1d) for Coconino sandstone and equation (A3d) for Bentheim sandstone) for comparison. The variations of dilatancy factor  $\beta$  at pure shear ( $\theta = 0^\circ$ ) with  $\sigma_{\text{oct},f}$  are also displayed.

With the determined value of  $\alpha$  in equation (5), the failure plane angles could be predicted and compared with the experimental data obtained in the novel loading path tests. The use of this angle description is then extended to predicting the variation of  $\theta$  with  $\sigma_2$  for constant  $\sigma_3$  and compared with experimental results in the common loading path tests (constant  $\sigma_2$  and  $\sigma_3$ ) [see Ma and Haimson, 2016]. This comparison is based on the hypothesis that angle's variation with  $\sigma_2$  for a constant  $\sigma_3$  can be described by the change in the applied Lode angle ( $\theta$ ) and the mean stress ( $\sigma_{\text{oct},f}$ ) determined from results based on the novel test observations.

## 4.2. Prediction Results

### 4.2.1. Coconino Sandstone

As shown in Figure 5a, the resulting  $\mu$  first increased slightly for  $\sigma_{\text{oct},f} < 100$  MPa but then generally decreased with  $\sigma_{\text{oct},f}$ . Despite the initial rise, the trend of the derived  $\mu$  was qualitatively consistent with that revealed by the experiments. The magnitude of the derived  $\mu$  was, however, significantly larger than the experimental value, except for the higher values of  $\sigma_{\text{oct},f}$ . The decrease of frictional coefficient with  $\sigma_{\text{oct},f}$  was expected for porous, compactive sandstone [Wong and Baud, 2012]. The trend and magnitude of the inferred dilatancy factor  $\beta$  values were reasonable. In particular, they showed a monotonic decrease from nearly 0.3 at  $\sigma_{\text{oct},f} = 50$  MPa to about  $-0.5$  at  $\sigma_{\text{oct},f} = 400$  MPa. The relatively large decrease of  $\beta$  apparently compensated for the initial increase of  $\mu$ , causing the sum of  $(\beta + \mu)$  to generally decrease with  $\sigma_{\text{oct},f}$ . This is consistent with the observation that  $(\beta + \mu)$  and the failure plane angle  $\theta$  decreased with  $\sigma_{\text{oct},f}$ . It is, however, important to mention that Figure 5a only depicts the case of the deviatoric pure shear ( $\theta = 0^\circ$ ), and the variations of frictional coefficient and dilatancy factor with  $\sigma_{\text{oct},f}$  are different under other Lode angles. The functions of  $H'(\sigma) \cdot \tau_0$  and  $d\tau_0/d\sigma$  were then substituted into equation (5) to compute the theoretically predicted failure plane angle ( $\theta$ ) for all experimental stress conditions at failure.

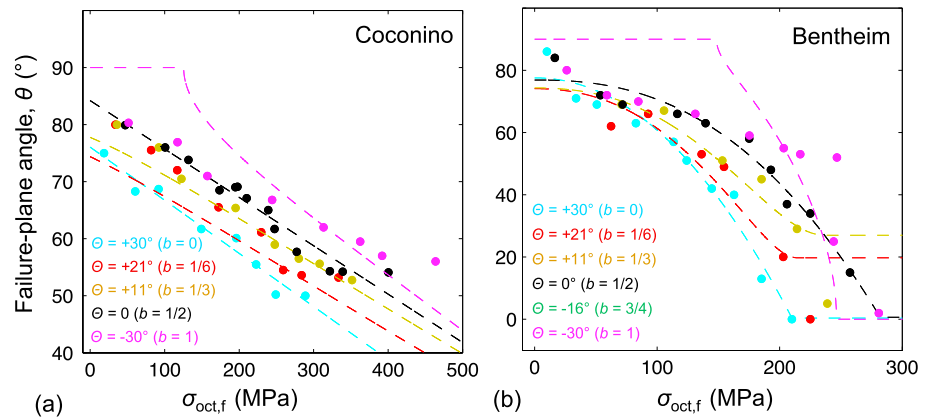


**Figure 6.** Predicted variation of the failure plane angle  $\theta$  with the mean stress at failure ( $\sigma_{oct,f}$ ) for all constant Lode angles in Coconino and Bentheim sandstones against experimental data (discrete points), indicating the brittle-ductile transition.

**4.2.1.1. Novel Loading Path**

Table 2 presents the point-to-point comparison between the testing results and the predictions for each constant  $\sigma_3$ . The predicted angle  $\theta$  generally matched the experimentally obtained values within  $\pm 5^\circ$ . Figure 6a shows the predicted variation of  $\theta$  with  $\sigma_{oct,f}$  for all applied Lode angles. The prediction in general is in reasonable agreement with the trend obtained in the experiments: for a constant Lode angle, the failure plane angle declined consistently with the rise in  $\sigma_{oct,f}$ , and for a constant  $\sigma_{oct,f}$ , angle increased as the Lode angle  $\theta$  varied from  $+30^\circ$  to  $-30^\circ$ .

The predicted failure plane angles  $\theta$  matched well the measured angles  $\theta$  for axisymmetric compression ( $\theta = +30^\circ$ , or  $\sigma_2 = \sigma_3$ ) and pure shear ( $\theta = 0^\circ$ ). This was expected since these two test series served as the input of the prediction (Text S2, equations (A1) and (A3)). Predicted  $\theta$  approximated reasonably well experimental values at other Lode angles, except for axisymmetric extension ( $\theta = -30^\circ$ ;  $\sigma_2 = \sigma_1$ ). For the test series in which  $\theta > 0$  (i.e.,  $\theta = +21^\circ$  and  $+11^\circ$ ), the model underestimated the failure plane angle by about  $8^\circ$  at low  $\sigma_{oct,f}$  ( $< 50$  MPa) and predicted a less inclined  $\theta$  versus  $\sigma_{oct,f}$  trend than what was observed experimentally. Thus, the discrepancy diminished as  $\sigma_{oct,f}$  approached the highest  $\sigma_{oct,f}$  ( $= 465$  MPa). For the test series at  $\theta = -30^\circ$  ( $\sigma_2 = \sigma_1$ ), the predictions yielded a  $90^\circ$  angle, corresponding to a dilation band, for  $\sigma_{oct,f} < \sim 120$  MPa, overestimating the experimental value by nearly  $10^\circ$ . As  $\sigma_{oct,f}$  was further increased, the model proved to be inferior: the predicted angle variation with  $\sigma_{oct,f}$  is much more significant than the measured angle.

**4.2.1.2. Common Loading Path**

The true triaxial tests using the common loading path [Ma and Haimson, 2016] revealed a consistent variation of failure plane angle with  $\sigma_2$  for constant  $\sigma_3$ . We predicted the failure plane angle under constant  $\sigma_2$  and  $\sigma_3$  to compare with the experimental observations and to evaluate the applicability of the three-invariant model to this context.

We used the empirically fitted  $\sigma_{1,peak}$  versus  $\sigma_2$  trends by Ma and Haimson [2016] as the input values. Then the predicted failure plane angles for all  $\sigma_3$  levels were compared with the discrete experimental data points (Figure 7). The prediction demonstrated the effect of  $\sigma_2$  on the rise of the failure plane angle for a constant  $\sigma_3$ . The theoretical prediction overestimated the measured angle for  $\sigma_3 \leq 20$  MPa, but it substantially improved as  $\sigma_3$  was raised. At low to intermediate  $\sigma_3$  level (between 50 and 100 MPa), the predicted  $\theta$  first slightly declined as  $\sigma_2$  was raised beyond  $\sigma_3$ , then consistently rose until  $\sigma_2 = \sigma_1$ , though at a decreasing rate. It appeared that the angle rise with  $\sigma_2$  gradually diminished as  $\sigma_3$  was raised. At high  $\sigma_3$  level (between 100 and 150 MPa), the angle eventually reached a maximum and then declined for larger  $\sigma_2$ .

**4.2.2. Bentheim Sandstone**

The three-invariant model prediction of the failure plane angle in Bentheim sandstone was performed via the same procedure as in Coconino sandstone. Figure 5b shows the variations of  $\mu$  and  $\beta$  at pure shear stress state with  $\sigma_{oct,f}$ .  $\mu$  was also compared with the experimentally obtained  $\mu^E$ . Despite a negligible rise for  $\sigma_{oct,f} < 15$  MPa, the derived  $\mu$  increased from about 1 at  $\sigma_{oct,f} = 20$  MPa to approximately 7 at

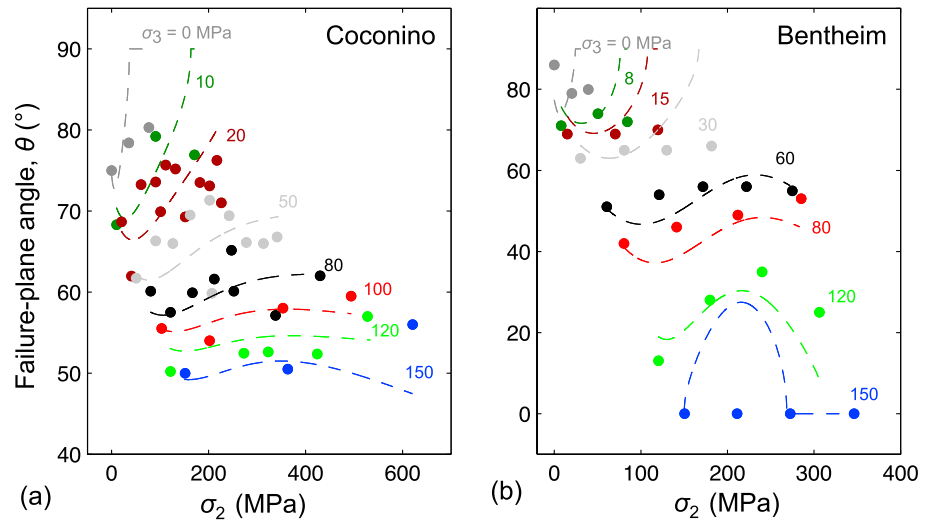


**Figure 7.** Failure plane angle ( $\theta$ ) variation with  $\sigma_2$  for all constant  $\sigma_3$  levels in Coconino and Bentheim sandstones tested under the common loading path: the three-invariant model predictions (dashed curves) and the experimentally observed angles (data points).

$\sigma_{oct,f} = 150$  MPa. The value of  $\mu$  at low  $\sigma_{oct,f}$  was in qualitative agreement with the experimentally obtained  $\mu^E$ , but the variations of  $\mu$  surprisingly trended opposite to the experimental variation. The increasing  $\mu$ , although appearing to flatten at  $\sigma_{oct,f} = 150$  MPa, is not consistent with the emergence of cap on the experimental  $\tau_{oct,f}$  versus  $\sigma_{oct,f}$  curve (see section 4.2.3 for discussion). The values of the dilatancy factor  $\beta$  decreased monotonically with  $\sigma_{oct,f}$ , showing an excessive drop from about 0 at  $\sigma_{oct,f} = 20$  MPa to about  $-8$  at  $\sigma_{oct,f} = 150$  MPa, suggesting very strong compaction. Given the idealizations of the model and dispersion in the data, the derived values of  $\beta$  and  $\mu$  have questionable significance.  $\beta$  and  $\mu$  compensated each other so that the sum of  $(\beta + \mu)$  generally decreased with  $\sigma_{oct,f}$ , consistent with the fact that failure plane angle  $\theta$  decreased with  $\sigma_{oct,f}$ .

The constrained functions of  $H(\sigma) \cdot \tau_0$  and  $d\tau_0/d\sigma$  were used to determine the exact form of equation (5) and then to compute the failure plane angle ( $\theta$ ) for all the stress conditions at failure in the experiments of both novel and common loading paths.

#### 4.2.2.1. Novel Loading Path

The angle prediction for Bentheim sandstone using the novel loading path is shown in Table 2 for point-to-point comparison, and in Figure 6 for the continuous trend. Since the axisymmetric compression ( $\theta = +30^\circ$ ) and pure shear ( $\theta = 0^\circ$ ) test data series were employed in the prediction process, predicted  $\theta$  at these two Lode angles matched the experimental data. Predicted  $\theta$  approximated reasonably well experimental values at other Lode angles ( $\theta = +21^\circ, +11^\circ$ , and  $-16^\circ$ ). At the highest values of  $\sigma_{oct,f}$  compaction bands ( $\theta = 0^\circ$ ) are predicted for all Lode angles except  $\theta = 0^\circ$ .

In the test series conducted at  $\theta = -30^\circ$  ( $\sigma_2 = \sigma_1$ ) and  $\sigma_{oct,f} < \sim 150$  MPa, the prediction yielded a  $90^\circ$  angle (corresponding to the formation of dilation band), overestimating measured  $\theta$  by nearly  $20^\circ$ . As  $\sigma_{oct,f}$  was further increased, the prediction improved, but the predicted angle declined much more rapidly with  $\sigma_{oct,f}$  than the experimental observation. Figure 6 represents the predicted variation of  $\theta$  with  $\sigma_{oct,f}$  for all constant Lode angles. Generally, the prediction confirmed the trend obtained in the experiments: for a constant Lode angle, the failure plane angle declined consistently with the rise in  $\sigma_{oct,f}$ , and for a constant  $\sigma_{oct,f}$  the angle increased as the Lode angle increased from  $+30^\circ$  to  $-30^\circ$ .

#### 4.2.2.2. Common Loading Path

Figure 7b depicts a comparison between testing results and predictions for each constant  $\sigma_3$  (test data taken from *Ma and Haimson [2016]*). For the same stress condition at failure ( $\sigma_{1,peak}, \sigma_2, \sigma_3$ ), the predicted angle is within  $8^\circ$  from the experimentally obtained magnitude. The prediction demonstrates a direct relationship between  $\sigma_2$  and the failure plane angle  $\theta$  for a constant  $\sigma_3$ , and a seemingly diminishing rise with  $\sigma_2$  as  $\sigma_3$  was raised. Notably, at high  $\sigma_3$  level (between 120 and 150 MPa), the prediction yielded a nearly parabolic

trend: angle quickly rose to a maximum at some intermediate  $\sigma_2$  level and then declined for larger  $\sigma_2$  (Figure 7b).

#### 4.2.3. Discussion

The predictions for the failure plane angle using the three-invariant model agree qualitatively with the experimental data for both sandstones. As expected, the predictions were in excellent agreement with the experimental results at both Lode angles  $0^\circ$  and  $+30^\circ$ . The use of two novel test data subsets provided the variation of failure plane angle ( $\theta$ ) with the Lode angle  $\Theta$ . The predictions are promising in the common tests as well. The predicted  $\theta$  versus  $\sigma_2$  trend for each constant  $\sigma_3$  generally agreed with the experimental results and a seemingly diminishing  $\sigma_2$  effect with increasing  $\sigma_3$  observed in the tests was replicated.

However, the discrepancy at the axisymmetric extension state ( $\Theta = -30^\circ$ , or  $\sigma_2 = \sigma_1$ ) was significant. The model consistently predicted a dilation band ( $\theta = 90^\circ$ ) at low to intermediate levels of  $\sigma_{\text{oct},f}$  contrary to the experimentally observed high-angle shear bands. It is possible that the imperfect testing conditions (such as end effects, friction, unbalanced loading) may induce a shear failure rather than axial splitting at extremely low confining pressure. But it is unlikely that the dilation bands would develop under  $\sigma_3$  of up to 30 MPa in Bentheim sandstone. As a consequence, the overall prediction should not be assigned more than qualitative significance at low values of  $\sigma_3$ .

Although the dilatancy factor  $\beta$  is not measured in the experiments, it is calculated from equation (13b). The variation for Coconino sandstone is reasonable: it decreases from a value of about 0.3 to about  $-0.5$  with an increase in  $\sigma_{\text{oct},f}$  corresponding to a change from dilation to compaction. For the Bentheim sandstone, the trend of decreasing  $\beta$  with  $\sigma_{\text{oct},f}$  is reasonable but the magnitude is unrealistically large for the larger values of  $\sigma_{\text{oct},f}$ . For the Coconino sandstone the variation of the inferred friction coefficient  $\mu$  is roughly consistent with the variation of the experimental value  $\mu^E$  except for a slightly portion at the lower values of  $\sigma_{\text{oct},f}$ . The magnitude is, however, larger than the experimental value. For the Bentheim sandstone, the variation of  $\mu$  is unexpected: it increases with  $\sigma_{\text{oct},f}$  to a large value at higher  $\sigma_{\text{oct},f}$ . A decrease corresponding to a transition to a cap is expected (and exhibited by the experimental value). A similar anomalous increase, though not so large, was also obtained by *Haimson and Rudnicki* [2010]. Despite these discrepancies and unexpected results, the agreement of the calculated and observed values of the failure plane angle is reasonable.

There are a number of possible factors that could contribute to the discrepancies. One is that the use of failure data instead of the yield data caused a different  $\tau_{\text{oct},f}$  versus  $\sigma_{\text{oct},f}$  trend, which can induce the discrepancy in deriving the material parameters. The unrealistic variation of frictional coefficient with  $\sigma_{\text{oct},f}$  in Bentheim sandstone could be partly due to the uncertainty of failure plane angle measurements at high  $\sigma_{\text{oct},f}$ . Unlike the induced shear fractures in Coconino sandstone, the orientation of the diffuse shear-enhanced compaction bands in Bentheim sandstone were difficult to measure. This uncertainty can influence the prediction because of the use of equation (A4) as inputs. Another factor is the restriction of the parameter  $A$  to be a constant in the predictions. The trend that  $A$  declines monotonically with  $\sigma_{\text{oct},f}$  is generally the case revealed experimentally [*Ma et al.*, 2014, 2017]. It is unclear to what extent the discrepancy between the experimental data and predictions might be due to taking  $A$  as a constant, but a more sophisticated representation of parameter  $A$  would compromise the simplicity of the prediction procedure. The effect of  $A$  is worth investigating in our future work.

Despite the weaknesses of the model, the use of the bifurcation theory to model the failure plane angle demonstrated that the effects of the Lode angle and the mean stress on fault plane angle seem to be adequate to represent the variation of failure plane angle with  $\sigma_2$  for a constant  $\sigma_3$ .

## 5. Concluding Remarks

We have conducted true triaxial experiments in two porous sandstones using a novel loading path that maintains constant the Lode angle  $\Theta$ . The test results revealed the respective contributions of Lode angle and mean stress to failure stress, failure plane angle, and failure mode. Common to both sandstones is that the octahedral shear stress required for failure increases with both mean stress and Lode angle when shear failure mode dominates. However, the dependency of failure on mean stress and Lode angle is reversed when compactive failure mode is in control. The compactive failure mode corresponds to the cap regime in the  $\tau_{\text{oct},f}$ - $\sigma_{\text{oct},f}$  space, in which  $\tau_{\text{oct},f}$  decreases with the increase in  $\sigma_{\text{oct},f}$ . The compactive failure mode

was evident in the high-porosity Bentheim sandstone when subjected to high mean stress, creating compaction bands. The Coconino sandstone did not enter the compactive failure regime within the maximum  $\sigma_3$  applied. Bentheim sandstone appears to be more susceptible to compaction mainly due to its higher porosity.

In both sandstones, the failure plane angle monotonically decreases with mean stress and also decreases when Lode angle rises from  $-30^\circ$  and  $+30^\circ$ . For Coconino sandstone, failure plane angle varied between  $80^\circ$  and  $50^\circ$  while for Bentheim sandstone the angle dropped to  $0^\circ$  (pure compaction bands) at high mean stress. Along with the decrease in failure plane angle, the appearance of failure planes evolved in both sandstones, signifying a brittle-ductile transition. The transition was significantly affected by the increase of mean stress for a constant Lode angle.

We sought a theoretical comparison to our experimental failure trend. Following Rudnicki [2013], we employed an updated version of bifurcation theory from Rudnicki and Rice [1975] by including a three-invariant failure description to model the failure plane angle variation. The theoretical prediction for novel loading path tests is in good agreement with the experimental data by faithfully representing the failure plane angle variation with mean stress and Lode angle. The model was then extended to predict the failure plane angle variation with  $\sigma_2$  for constant  $\sigma_3$  [Ma and Haimson, 2016]. The experimental trend was qualitatively replicated by the theoretical predictions. This comparison suggests the variation of failure plane angle with  $\sigma_2$  could be fundamentally considered as a result of angle variation with both Lode angle and mean stress.

#### Acknowledgments

This research was supported by the National Science Foundation grant EAR-0940323 (for B.C.H. and X.M.) and grant EAR-0940981 (for J.W.R.). The authors thank the Editors and two anonymous reviewers for their critical comments that significantly improved the manuscript. Experimental data are available from the corresponding author upon request.

#### References

- Aydin, A., R. I. Borja, and P. Eichhubl (2006), Geological and mathematical framework for failure modes in granular rock, *J. Struct. Geol.*, *28*, 83–98.
- Bésuelle, P. (2001), Compacting and dilating shear bands in porous rocks: Theoretical and experimental conditions, *J. Geophys. Res.*, *106*, 13,435–13,442, doi:10.1029/2001JB900011.
- Bésuelle, P., and J. W. Rudnicki (1997), Localization: shear bands and compaction bands, in *Mechanics of Fluid Saturated Rock, International Geophysics Series*, vol. 89, edited by Y. Guéguen and M. Boutéca, pp. 219–321, Elsevier, Boston, Mass.
- Bésuelle, P., J. Desrués, and S. Raynaud (2000), Experimental characterisation of the localisation phenomenon inside a Vosges sandstone in a triaxial cell, *Int. J. Rock Mech. Min. Sci.*, *37*, 1223–1237.
- Bobich, J. K. (2005), Experimental analysis of the extension to shear fracture transition in Berea Sandstone, MS thesis, 52 pp., Texas A&M Univ.
- Borja, R. I. (2013), *Plasticity: Modeling & Computation*, Springer, Heidelberg, doi:10.1007/978-3-642-38547-6.
- Brace, W. F., and D. L. Kohlstedt (1980), Limits on lithospheric stress imposed by laboratory experiments, *J. Geophys. Res.*, *85*(B11), 6248–6252, doi:10.1029/JB085iB11p06248.
- Du Bernard, X., P. Eichhubl, and A. Aydin (2002), Dilation bands: A new form of localized failure in granular media, *Geophys. Res. Lett.* *29*(24), 2176. doi:10.1029/2002GL015966.
- Duan, K., F. Kwok, and X. Ma (2016), DEM simulations of sandstone under true triaxial compressive tests, *Acta Geotech.*, doi:10.1007/s11440-016-0480-6.
- Eichhubl, P., J. N. Hooker, and S. E. Laubach (2010), Pure and shear-enhanced compaction bands in Aztec Sandstone, *J. Struct. Geol.*, *32*, 1873–1886.
- Fossen, H., R. A. Schultz, and A. Torabi (2011), Conditions and implications for compaction band formation in the Navajo Sandstone, Utah, *J. Struct. Geol.*, *33*, 1477–1490.
- Haimson, B. (2006), True triaxial stresses and the brittle fracture of rock, *Pure Appl. Geophys.*, *163*, 1101–1130.
- Haimson, B., and J. W. Rudnicki (2010), The effect of the intermediate principal stress on fault formation and fault angle in siltstone, *J. Struct. Geol.*, *32*, 1701–1711.
- Haimson, B., C. Chang and X. Ma (2016), True triaxial testing of rocks and the effect of the intermediate principal stress on failure characteristics, in *Rock Mechanics and Engineering*, vol. 1, chap. 13, edited by X.-T. Feng, pp. 379–396, CRC Press, Leiden, Netherlands.
- Haimson, B. C. (1978), The hydrofracturing stress measuring method and recent field results, *Int. J. Rock Mech. Min. Sci. Geomech. Abstr.*, *15*, 167–178.
- Holcomb, D. J., and W. A. Olsson (2003), Compaction localization and fluid flow, *J. Geophys. Res.* *108*(B6), 2290, doi:10.1029/2001JB000813.
- Holcomb, D., J. W. Rudnicki, K. A. Issen, and K. Sternlof (2007), Compaction localization in the Earth and the laboratory: State of the research and research directions, *Acta Geotech.*, *2*, 1–15.
- Ingraham, M. D., K. A. Issen, and D. J. Holcomb (2013), Response of Castlegate sandstone to true triaxial states of stress, *J. Geophys. Res. Solid Earth*, *118*, 536–552, doi:10.1002/jrb.50084.
- Issen, K. A., and J. W. Rudnicki (2000), Conditions for compaction bands in porous rock, *J. Geophys. Res.*, *105*(B9), 21,529–21,536, doi:10.1029/2000JB900185.
- Jimenez, R., and X. Ma (2013), A note on the strength symmetry imposed by Mogi's true-triaxial criterion, *Int. J. Rock Mech. Min. Sci.*, *64*, 17–21, doi:10.1016/j.ijrmm.2013.08.009.
- Klein, E., P. Baud, T. Reuschlé, and T.-F. Wong (2001), Mechanical behavior and failure mode of Bentheim sandstone under triaxial compression, *Phys. Chem. Earth (A)*, *26*, 21–25.
- Labuz, J. F., R. Y. Makhnenko, and J. T. Harvieux (2016), Failure criterion with intermediate stress and two friction angles, ARMA paper 16-620 presented at 50th U.S. Rock Mechanics Geomechanics Symposium, Houston, Tex., 26–29 June.
- Lade, P. V., and J. M. Duncan (1975), Elastoplastic stress-strain theory for cohesionless soil, *J. Geotech. Eng. Div. ASCE*, *101*(GT10), 1037–1053.
- Lee, H. (2005), Borehole breakouts in arkosic sandstones and quartz-rich sandstones, PhD thesis, 240 pp., Univ. of Wisconsin-Madison.

- Ma, X. (2014), Failure characteristics of compactive, porous sandstones subjected to true triaxial stresses, PhD thesis, 308 pp., Univ. of Wisconsin-Madison.
- Ma, X., and B. Haimson (2016), Failure characteristics of two porous sandstones subjected to true triaxial stresses, *J. Geophys. Res. Solid Earth*, *121*, 6477–6498, doi:10.1002/2016JB012979.
- Ma, X., J. W. Rudnicki, and B. Haimson (2014), True triaxial tests in two porous sandstones: Experimental failure characteristics and theoretical prediction, ARMA paper 14-7286 presented at 48th U.S. Rock Mechanics Geomechanics Symposium, Minneapolis, 1–4 June.
- Ma, X., J. Rudnicki, and B. Haimson (2017), The application of a modified Lade-Duncan-Matsuoka-Nakai failure criterion to two porous sandstones, *Int. J. Rock Mech. Min. Sci.*, *92*, 9–18, doi:10.1016/j.ijrmmms.2016.12.004.
- Makhnenko, R. Y., and J. F. Labuz (2014), Plane strain testing with passive restraint, *Rock Mech. Rock Eng.*, *47*, 2021–2029, doi:10.1007/s00603-013-0508-2.
- Makhnenko, R. Y., J. Harvieux, and J. F. Labuz (2015), Paul-Mohr-Coulomb failure surface of rock in the brittle regime, *Geophys. Res. Lett.*, *42*, 6975–6981, doi:10.1002/2015GL065457.
- Matsuoka, H., and T. Nakai (1974), Stress-deformation and strength characteristics of soil under three different principal stresses, *Proc. Jpn. Soc. Civ. Eng.*, *232*, 59–70.
- McGarr, A., and N. C. Gay (1978), State of stress in the Earth's crust, *Annu. Rev. Earth Planet. Sci.*, *6*, 405–436.
- Meyer, J. P., and J. F. Labuz (2013), Linear failure criteria with three principal stresses, *Int. J. Rock Mech. Min. Sci.*, *60*, 180–187, doi:10.1016/j.ijrmmms.2012.12.040.
- Mogi, K. (2007), *Experimental Rock Mechanics*, 361 pp., Belkma, London.
- Mollema, P. N., and M. A. Antonellini (1996), Compaction bands: A structural analog for anti-mode I cracks in aeolian sandstone, *Tectonophysics*, *267*, 209–228.
- Olsson, W. A. (1999), Theoretical and experimental investigation of compaction bands in porous rock, *J. Geophys. Res.*, *104*(B4), 7219–7228, doi:10.1029/1998JB900120.
- Ottosen, N. S., and K. Runesson (1991), Properties of discontinuous bifurcation solutions in elasto-plasticity, *Int. J. Solids Struct.*, *27*, 401–421.
- Paterson, M. S., and T.-F. Wong (2005), *Experimental Rock Deformation—The Brittle Field*, 2nd ed., 347 pp., Springer, New York.
- Rudnicki, J. W. (2008), Localized failure in brittle rock, in *Proceedings of the 3rd International Symposium on Thermo-Hydromechanical-Chemical Coupling in Geomaterials and Applications, GeoProc 2008*, edited by J.-F. Shao and N. Burlion, pp. 25–40, Wiley, London.
- Rudnicki, J. W. (2013), Failure of rocks in the laboratory and in the Earth, in *Proceedings of 22nd International Congress on Theoretical and Applied Mechanics Adelaide, Australia 24–29 August, 2008*, edited by J. P. Denier and M. D. Finn, pp. 199–215, Springer, Dordrecht, Netherlands.
- Rudnicki, J. W. (2016), A three invariant model of true triaxial tests on Castlegate sandstone, abstract MR43A-03, Fall Am. Geophys. Meet.
- Rudnicki, J. W., and J. R. Rice (1975), Conditions for the localization of deformation in pressure-sensitive dilatant materials, *J. Mech. Phys. Solids*, *23*, 371–394.
- Rudnicki, J. W., and W. A. Olsson (1998), Reexamination of fault angles predicted by shear localization theory, *Int. J. Rock Mech. Min. Sci.*, *35*, 4–5.
- Sternlof, K. R., J. R. Chapin, D. D. Pollard, and L. J. Durlofsky (2004), Permeability effects of deformation band arrays in sandstone, *Am. Assoc. Petrol. Geol. Bull.*, *88*, 1315–1329.
- Sternlof, K. R., J. W. Rudnicki, and D. D. Pollard (2005), Anticrack inclusion model for compaction bands in sandstone, *J. Geophys. Res.*, *110*, B11403, doi:10.1029/2005JB003764.
- Sun, W., J. E. Andrade, J. W. Rudnicki, and P. Eichhubl (2011), Connecting microstructural attributes and permeability from 3D tomographic images of in situ shear-enhanced compaction bands using multiscale computations, *Geophys. Res. Lett.*, *38*, L10302, doi:10.1029/2011GL047683.
- Vajdova, V., P. Baud, and T.-f. Wong (2004), Permeability evolution during localized deformation in Bentheim sandstone, *J. Geophys. Res.*, *109*, B10406, doi:10.1029/2003JB002942.
- Vernik, L., and M. Zoback (1992), Estimation of maximum horizontal principal stress magnitude from stress-induced well bore breakouts in the Cajon Pass Scientific Research Borehole, *J. Geophys. Res.*, *97*(B4), 5109–5119, doi:10.1029/91JB01673.
- Wong, T.-f., and P. Baud (2012), The brittle-ductile transition in porous rock: A review, *J. Struct. Geol.*, *44*, 25–53.
- Zhu, W., L. G. J. Montesi, and T.-f. Wong (1997), Shear-enhanced compaction and permeability reduction: Triaxial extension tests on porous sandstone, *Mech. Mater.*, *25*, 199–214.